J. Fluid Mech. (2018), *vol.* 834, *pp.* 125–148.
doi:10.1017/jfm.2017.646

Application of a model of internal hydraulic jumps

S. A. Thorpe[1,†], J. Malarkey[1], G. Voet[2], M. H. Alford[2], J. B. Girton[3] and G. S. Carter[4]

[1]School of Ocean Sciences, Bangor University, Menai Bridge, Anglesey LL59 5AB, UK

[2]Scripps Institution of Oceanography, University of California, San Diego, CA 92093, USA

[3]Applied Physics Laboratory, University of Washington, Seattle, WA 98105, USA

[4]Department of Oceanography, University of Hawaii, Honolulu, HI 96822, USA

(Received 25 March 2017; revised 28 July 2017; accepted 9 September 2017)

A model devised by Thorpe & Li (*J. Fluid Mech.*, vol. 758, 2014, pp. 94–120) that predicts the conditions in which stationary turbulent hydraulic jumps can occur in the flow of a continuously stratified layer over a horizontal rigid bottom is applied to, and its results compared with, observations made at several locations in the ocean. The model identifies two positions in the Samoan Passage at which hydraulic jumps should occur and where changes in the structure of the flow are indeed observed. The model predicts the amplitude of changes and the observed mode 2 form of the transitions. The predicted dissipation of turbulent kinetic energy is also consistent with observations. One location provides a particularly well-defined example of a persistent hydraulic jump. It takes the form of a 390 m thick and 3.7 km long mixing layer with frequent density inversions separated from the seabed by some 200 m of relatively rapidly moving dense water, thus revealing the previously unknown structure of an internal hydraulic jump in the deep ocean. Predictions in the Red Sea Outflow in the Gulf of Aden are relatively uncertain. Available data, and the model predictions, do not provide strong support for the existence of hydraulic jumps. In the Mediterranean Outflow, however, both model and data indicate the presence of a hydraulic jump.

Key words: hydraulic control, stratified flows, turbulent flows

1. Introduction

Little is known of the form and structure of hydraulic jumps in the deep ocean, and until recently measurements in and around features that satisfy the dynamical conditions necessary for hydraulic transitions to occur have been lacking. The potential importance of hydraulic jumps as a mechanism for mixing in stratified near-bed currents is, however, recognized, and several studies have been made of the flow in regions where jumps might be expected, notably in the Romanche Fracture Zone (Polzin *et al.* 1996) and in the near-bottom outflows from both the Red Sea (Peters &

† Email address for correspondence: s.a.thorpe@bangor.ac.uk

Johns 2005; Peters *et al.* 2005) and the Mediterranean Sea (Gasser *et al.* 2011; Nash *et al.* 2012). Alford *et al.* (2013) conclude that hydraulic jumps form downstream of a sill in the Samoan Passage, resulting in turbulent mixing. In the atmosphere, transitions in pressure, wind speed and potential temperature described as being caused by hydraulic jumps have been observed, for example, in the lee of the Sierra Nevada mountain range in California by Armi & Mayr (2011) and in katabatic winds in Adélie Land in Antarctica by Pettré & André (1991), the latter a manifestation of 'Loewe's phenomenon' (Baines 1995).

Our purpose here is to apply an idealized model in some of these regions where detailed measurements of near-bottom flows are available and jumps appear likely. The theoretical model predicts when flows are prone to hydraulic jumps and, if they are, the amplitude of jumps and what loss of energy occurs. The comparison with observations provides tests of the validity of the model and, within the limits of the model and its 'fit' to the data, examination of whether hydraulic jumps occur in observed flows and some indication of their nature.

The model is described in § 2, and applied to data in the following sections. Section 3 makes comparison with observations over and in the lee of a sill in the Samoan Passage. Two abrupt changes in the character of the flow are examined in detail and are identified as hydraulic jumps. In § 4 the model predictions are applied to observations in the Red Sea Outflow, whilst § 5 describes comparison of the model with observations in the Mediterranean Outflow. The main conclusions are discussed in § 6 and summarized in § 7.

2. The model

A theoretical model of a stationary turbulent internal hydraulic jump in a non-rotating system was devised by Thorpe & Li (2014, hereafter TL) and is illustrated in figure 1. A stratified layer in which the jump occurs flows over a rigid horizontal boundary at $z = 0$ and beneath a uniform stationary fluid of infinite depth. Unlike the majority of models of such jumps, which assume that the flow consists of two discrete uniform layers upstream of the hydraulic transition (reviewed, for example, by Baines (2016) and Ogden & Helfich (2016)), TL adopt continuous profiles of velocity and density both upstream and downstream of the transition. The velocities in the model are given by

$$u_i(z) = U_i F_i(z/h_i), \tag{2.1}$$

where $i = 1$ indicates a steady flow approaching a jump ('upstream') and $i = 2$ indicates a steady flow beyond the jump ('downstream') when turbulence generated within the region of the transition has collapsed, and h_i is the thickness of the flowing layers. The (positive) functions F_i are selected as 'η profiles'; for a given value η_i and with $y = z/h_i$,

$$F_i(y) = \begin{cases} 1, & \text{if } 0 \leqslant y \leqslant \eta_i \leqslant 1 \text{ (a uniform lower layer),} \\ (1-y)/(1-\eta_i), & \text{if } \eta_i \leqslant y \leqslant 1 \text{ (an interfacial layer),} \\ 0, & \text{if } y \geqslant 1 \text{ (a uniform and stationary upper layer).} \end{cases} \tag{2.2}$$

The η profiles provide examples of flows ranging from a uniform gradient extending from $z = 0$ to $z = h_i$ when $\eta_i = 0$ to a two-layer structure with discontinuity at $z = h_i$ when $\eta_i = 1$.

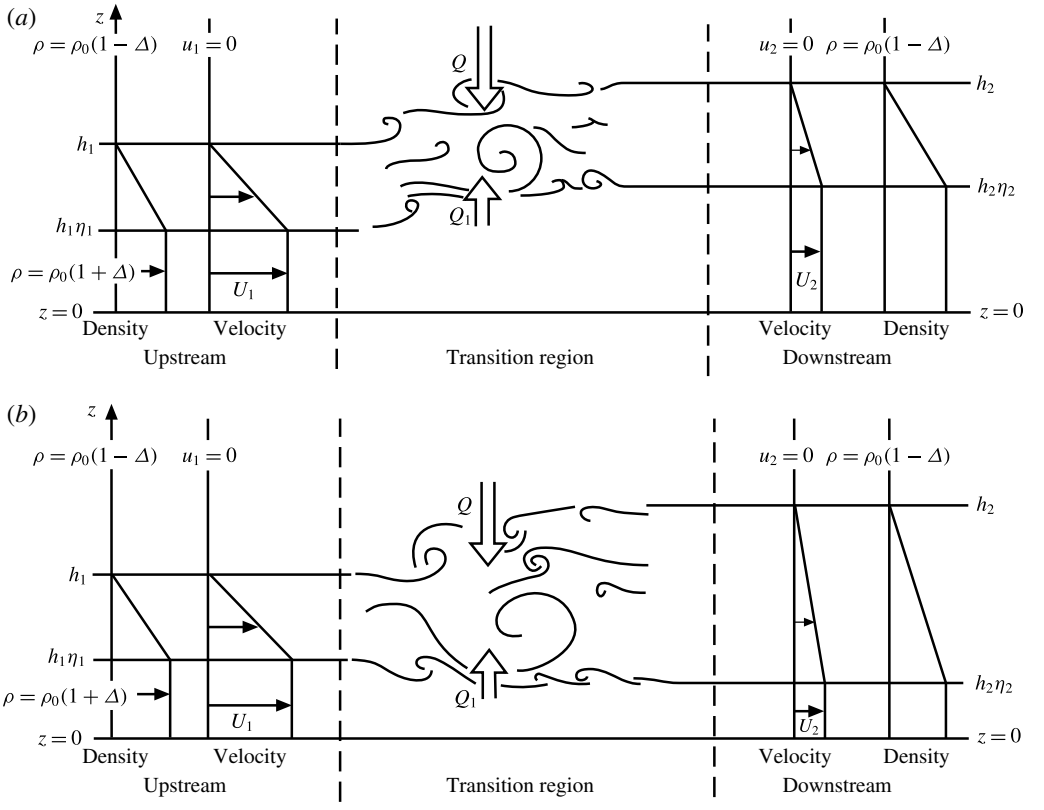

FIGURE 1. Sketches showing the model representation of a turbulent hydraulic jump or transition in a stratified shear flow over a plane boundary at $z = 0$: (*a*) a mode 1 transition and (*b*) a transition of mode 2. Here Q and Q_1 represent the fluxes of volume of density $\rho_0(1-\Delta)$ from above and of density $\rho_0(1+\Delta)$ from below into the transition zone. (From Thorpe & Li (2014); their figure 1.)

The density is chosen with a profile similar to the velocity:

$$\rho_i(z) = \rho_0[1 - \Delta + 2\Delta F_i(z/h_i)]. \tag{2.3}$$

The reference density, ρ_0, and the measure of density variation, Δ (and the velocity measures, U_i), are all positive. The density at the boundary, $z = 0$, is $\rho_0(1+\Delta)$ in the upstream flow and also in the downstream flow. (This requirement of equal densities at $z = 0$ can be relaxed to allow mixing in the transition to extend through the lower layer down to the seabed, so reducing the density in the downstream flow at $z = 0$ and introducing a measure, δ, of the density change, as described by Thorpe (2010) and TL.) The density gradients, $\mathrm{d}\rho_i/\mathrm{d}z$, are zero except in the interfacial layer, where they equal $-2\Delta\rho_0/[h_i(1-\eta_i)]$. Above $z = h_i$ the density is equal to $\rho_0(1-\Delta)$ and, since the density is uniform, no internal waves can propagate upwards from the transition region (but see appendix C). It is assumed that the transition is not undular; no allowance is made for mixing and energy loss in a train of stationary waves downstream of a jump. The downstream profiles defined by U_2, h_2 and η_2 depend on the turbulent mixing in the jump but are made to be consistent with their upstream values, U_1, h_1 and η_1, according to the laws of conservation of volume, mass and momentum fluxes.

The η profiles at locations upstream and downstream of perceived hydraulic jumps are fitted to the data as explained in appendix A to obtain values of η_i, U_i, h_i and $2\Delta\rho_0$. The gradient Richardson number in the interfacial layer ($\eta_i h_i < z < h_i$) is

$$Ri_i = 2g\Delta h_i(1-\eta_i)/U_i^2. \tag{2.4}$$

Closure is obtained by assuming that the downstream interfacial Richardson number, Ri_2, equals 1/3. This value is chosen because by the Miles–Howard theorem it ensures that the downstream flow is stable. Furthermore, it is well within the bounds of uncertainty of the final values, Ri_F, of Richardson numbers in laboratory and numerical studies of decaying turbulence following Kelvin–Helmholtz instability (KHI) in a stratified interfacial layer (e.g. Thorpe 1973; Smyth, Moum & Caldwell 2001). It should, however, be noted that whether there is a similar limiting Richardson number following the collapse of turbulence initiated in a hydraulic jump is not known, although a value of approximately 1/3 is indeed found downstream of the jumps analysed in § 3. The upstream flow is characterized by η_1 and a Froude number, Fr, defined as

$$Fr = U_1^2/(g\Delta h_1) = 2(1-\eta_1)/Ri_1. \tag{2.5}$$

Figure 2 summarizes the analysis of three factors important in internal hydraulic jumps: wave propagation, consistency with the conservation laws, and the stability of the upstream and downstream flows. It shows the character of flows satisfying the conservation laws and the possibility of transitions at points in the (η_1, Fr) plane defining the upstream flow. A necessary condition for a steady stationary jump is that no waves can propagate upstream to alter the flow in which the jump occurs. The bold lines of figure 2(*a*,*b*) are derived by Thorpe (2010, see his § 4.2) and indicate limiting values for this condition to apply. They mark the maximum value of Fr for given η_1 at which waves can propagate in the upstream direction; at greater values of Fr (when jumps can be stationary) there are no upstream-travelling waves. When $\eta_1 < 2/3$, the limiting Froude number equals $8(1-\eta_1)$ and (2.5) implies that $Ri_1 = 1/4$. (The condition $Ri_1 = 1/4$ is satisfied on the dashed line and on its continuation to $Fr = 8$ at $\eta_1 = 0$ in figure 2*a*,*b*.) Figure 2(*b*), found following TL, also shows where finite-amplitude jumps consistent with the conservation laws may be possible in given upstream flows, i.e. at points in the (η_1, Fr) plane. To the right of the bold line marking the limiting Fr, the plane is divided into three regions, A, B and C. No jumps are possible in region A. Just one solution of the conservation equations for a flow downstream of a jump is possible in region C (meaning that only one type of jump or mode of transition can occur). Two solutions exist in region B; one of two jumps are possible but only when η_1 exceeds 0.74 and Fr is sufficiently large. Jumps occur in the regions B and C where the upstream flow with corresponding η_1 and Fr is described as 'supercritical' to the formation of hydraulic jumps. Jumps are not supported in the remaining regions of the (Fr, η_1) plane; these flows are 'subcritical'. The smallest Fr at which a jump can occur is 2.2 when $\eta_1 = 0.74$, at the junction of regions B and C and the bold line. The single roots in region C generally correspond to mode 2 jumps (figure 1*b*) in which the interfacial layer in the upstream flow, $\eta_1 h_1 < z < h_1$, expands both upwards and downwards; values of h_2 exceed h_1 but $\eta_1 h_1 > \eta_2 h_2$, so that the upper isopycnals rise and the lower descend. The double roots of region B are either of mode 2 jumps or those of mode 1, in which all isopycnals rise through the transition as illustrated in figure 1(*a*).

The stability of the upstream flow was examined by TL (their § 2.2) and is summarized in figure 2(*c*). The hatched region shows where KHI is not possible in

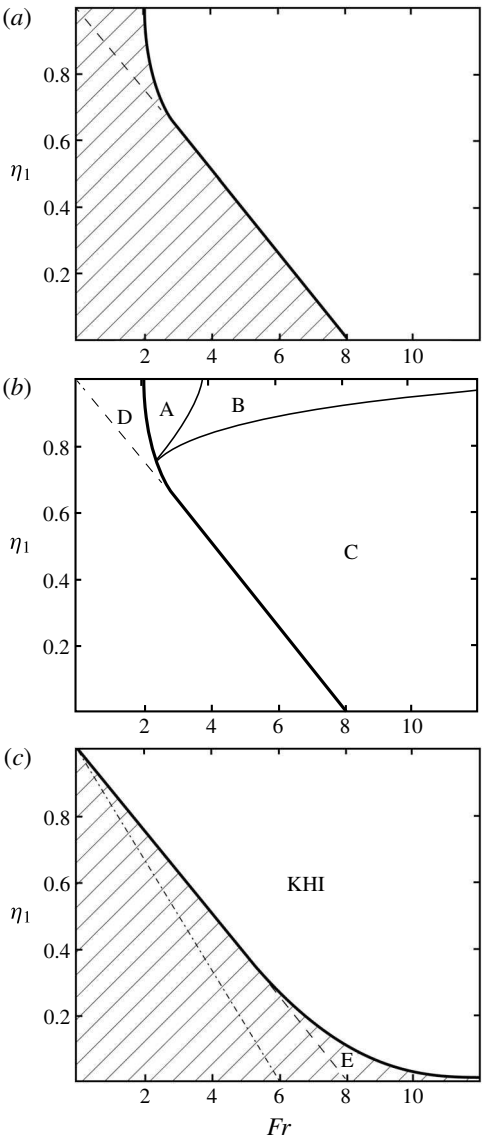

FIGURE 2. A summary of the stability of a flow and hydraulic jumps in the (η_1, Fr) plane. (*a*) Internal waves can propagate upstream in the hatched region, and consequently no stationary hydraulic jumps are formed here. One has $Ri = 1/4$ on the line joining ($\eta_1 = 0$, $Fr = 8$) to ($\eta_1 = 1$, $Fr = 0$), with smaller values of Ri to its right. (*b*) The region $Ri < 1/4$ is divided as follows: A, in which no jumps may occur; B, in which jumps of modes 1 and 2 are possible; and C, in which only one jump, generally of mode 2, is possible. Flows in B and C are supercritical and the remaining area of the (η_1, Fr) plane is subcritical. In D, $Ri < 1/4$ and the flow is unstable to KHI but, because waves can propagate upstream (as shown in panel (*a*)), no stationary jumps can occur. (*c*) The hatched region is where the flow is stable to KHI. Its boundary (thick line) is the stability boundary separating stable flow (to the left) from unstable flow (to the right). One has $Ri < 1/4$ in the stable region E at small η_1 to the right of the stability boundary where (as shown in panel (*b*)) hydraulic jumps may occur. The dot-dashed line corresponds to $Ri = 1/3$.

the upstream flow, i.e. where the Taylor–Goldstein equation describing the stability of small perturbations to the flow has no exponentially growing solutions. KHI may occur in the remaining region of the (η_1, Fr) plane. A value $Ri_1 = 1/3$ corresponds to the dot-dashed line, $Fr = 6(1 - \eta_1)$. Points on this line are to the left of, and outside, the supercritical regions B and C of figure 2(*b*) in which hydraulic jumps are possible: it follows that a steady downstream flow with Richardson number $Ri_2 = 1/3$ is therefore stable both to KHI and to a possible hydraulic transition whatever the value η_2. To be consistent with the model's assumption that $Ri_2 = 1/3$, a measured downstream Froude number should lie on (or at least be close to) the dotted line and be approximately equal to $6(1 - \eta_2)$. Although, by comparing figure 2(*b*,*c*), it is evident that KHI is possible where jumps may occur in all of region B and most of C, there is a small region marked E in figure 2(*c*), part of C, where jumps are possible but KHI is not. (The flow with small values of η_1 is stabilized by the presence of the rigid boundary at $z = 0$, reducing the critical Richardson number to values below 1/4.) The possibility of KHI where jumps occur in regions B and C implies that (unless the flow is in the region E) it might be difficult, if not impossible, when comparing model predictions to observations to distinguish between hydraulic transitions and those caused by KHI; the occurrence of turbulence and an associated change in flow profiles may be a consequence of a hydraulic transition or of KHI, and in this sense the two are synonymous. (It will, however, be shown in § 3 that in at least two cases the nature of the hydraulic transition is quite distinct from KHI.) In regions A and D of figure 2(*b*), the upstream flow is liable to KHI but not to a hydraulic jump, in D because upstream waves are possible (figure 2*a*) and in A because no hydraulic jump solutions can be found; for flows in region A, small-amplitude KHI disturbances may grow, but no finite-amplitude hydraulic transition is possible.

There is one factor that may distinguish hydraulic jumps from KHI. Where they occur, the turbulent hydraulic jumps are stationary, their position fixed where the flow becomes supercritical, e.g. downstream of sills or constrictions in the width of channels. The conditions favouring the onset of KHI may similarly be determined by the topography, e.g. by its enhancement of shear. It is, however, a property of KHI that the disturbances following instability and developing into billows and subsequently turbulence propagate downstream at a speed within the range of the flow speeds, i.e. so that a critical level exists. The billows propagate at a speed between that of the upper layer (zero in the model) and that of the lower layer, U_1, possibly causing the critical position from which they develop, i.e. where the flow becomes subject to KHI (and possibly supercritical), to pulsate slightly in its downstream location.

As explained further in § 3 (and shown later in figure 6), the TL model provides prediction of other quantities related to transitions. The theory does not establish, however, the physical processes leading to the onset of turbulence in the transition. These might include an overturning billow-like structure or rotor (Ogden & Helfich 2016; e.g. their figure 4*d* of an internal bore) or KHI. Nor does the theoretical model describe the nature of the flow within the turbulent transition (although it has been supposed to have a character sufficiently far downstream where turbulence has collapsed similar to that following KHI, with $Ri_2 = 1/3$). Much about its structure is, however, revealed by observations described in § 3. The model does not predict the values of η or Fr within the turbulent transition region itself, but these are determined from the observations. Some information is, however, available from the model about the mean rate of dissipation of turbulent kinetic energy as explained later, and estimates may be made of the vertical fluxes within the transition (Thorpe 2010).

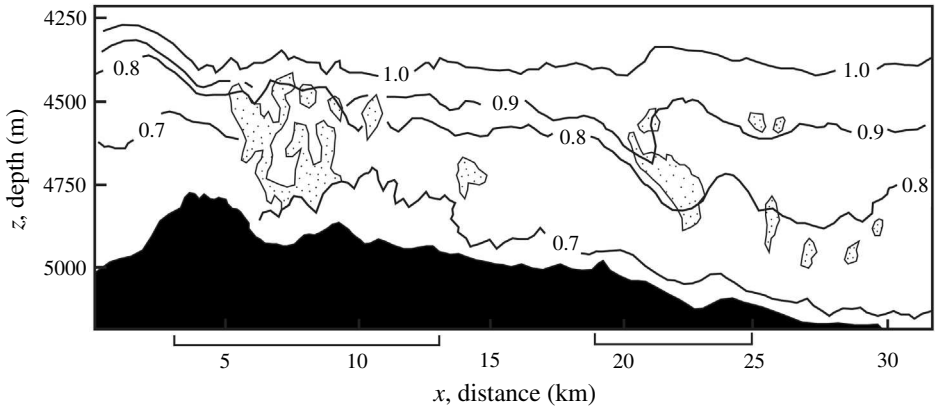

FIGURE 3. Contours of potential temperature (°C) and stippled regions in which the rate of dissipation of turbulent kinetic energy per unit mass computed using Thorpe scales exceeds 10^{-7} W kg^{-1} in a section through the Samoan Passage made while steaming at low speed in tow-yo mode (from Alford *et al.* (2013), figure 3*c*). The bottom topography is shown in black. The two sections, 19–25 km and 3–12 km (i.e. $x = 19$–25 and 3–12), selected for analysis in §§ 3.2 and 3.3, respectively, are marked on the horizontal distance axis.

Observations are used in §§ 3–5 to examine the predictions (and test the validity) of the theoretical model. Assumptions and approximations made in applying the theoretical model to observations are reviewed in appendix B. One of these is that, rather than the uniform density of the η profiles, the observed density profiles may have a nearly constant gradient above the flowing layer near the seabed (e.g. as seen later in profiles in figure 4*a*). It is shown in appendix C that this appears unlikely to allow upward radiation of internal waves with energy and momentum loss from a transition region.

3. The Samoan Passage

3.1. *The observations*

Alford *et al.* (2013) examined the dense deep northerly flow through the Samoan Passage. They made detailed 'tow-yo' measurements with a conductivity–temperature–depth (CTD) probe and a lowered acoustic Doppler current profiler (LADCP) to obtain profiles of potential density (sigma4, referenced to 4000 m) and velocity in a region of mean depth of approximately 5100 m. The 'tow-yo' cycled between 40 m off the bottom and 4200 m depth, making profiles with a derived 1 m vertical resolution approximately 250 m apart, and thus inclined at a mean angle to the horizontal of approximately 74°. Potential temperature and dissipation data over a major sill near 8° S are displayed in figure 3(*c*) in Alford *et al.*'s paper and are reproduced here in figure 3. Being at low latitude, the effects of the Earth's rotation are likely to be relatively small. This section shows locations designated by their position, x (in kilometres), from 0 to 31.5. It passes in a northerly direction from just upstream (south) of the sill. Adjacent to the seabed an approximately 250 m thick layer of relatively dense water flows northwards at ~ 0.4 m s^{-1}. It is capped by an interfacial layer in which the velocity and potential density decrease upwards. Above this, the flow is relatively small. The analysis made here is of two subsections of the data where hydraulic transitions appear likely. Section 3.2 describes $x = 19$ to 25, presented

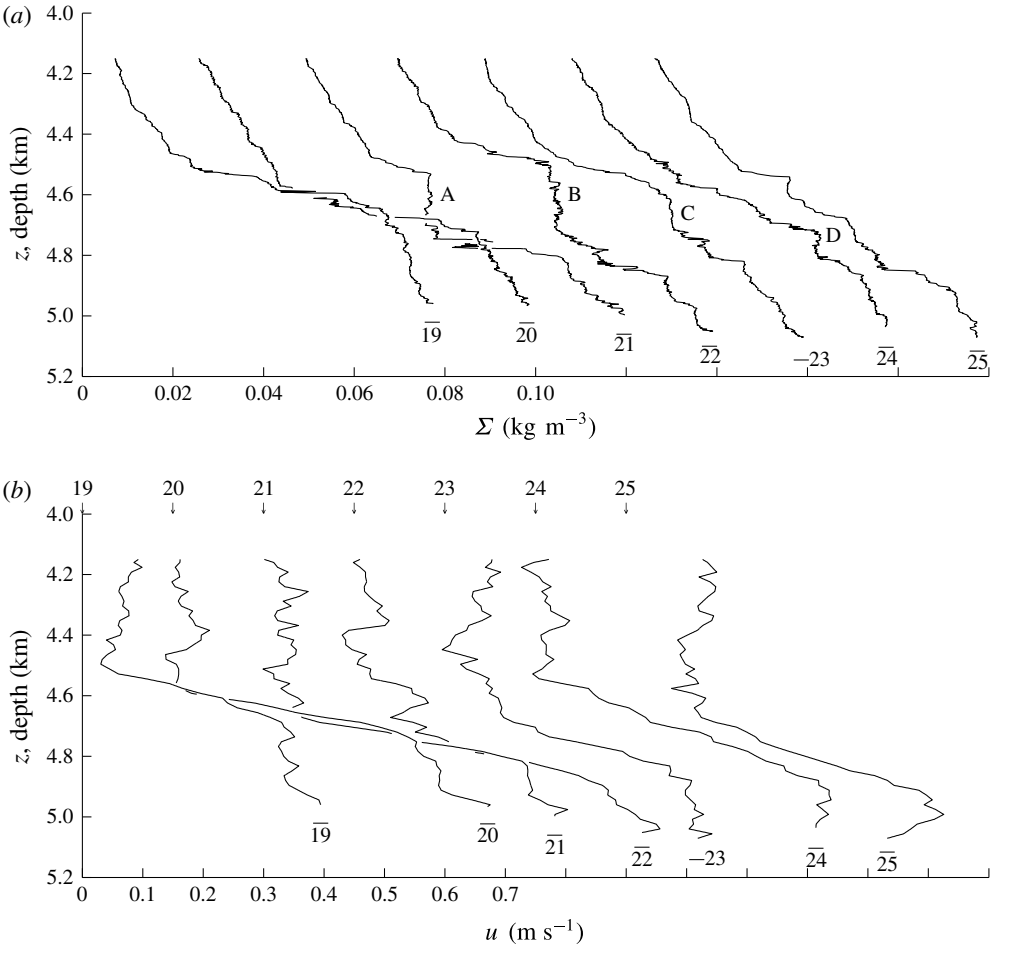

FIGURE 4. Profiles of (*a*) Σ, the potential density, measured in kg m^{-3}, minus 1045.9 kg m^{-3}, and (*b*) northward velocity, u, in m s^{-1}, in the Samoan Passage at roughly 1 km intervals from approximately $x = 19$ to $x = 25$. (The actual positions, the mean locations of the two-yo profiles, are $x = 19.1$, 20.1, 21, 22, 23.1, 24.1 and 25.2.) Successive profiles are displaced to the right by (*a*) 0.2 kg m^{-3} and (*b*) 0.15 m s^{-1}. The water depth is indicated by horizontal bars beneath each profile. The position of $u = 0$ for each profile is marked at the top of (*b*) by vertical arrows. The features marked A to D in (*a*) are discussed in the text.

first because (as it appears from figure 3) it is found to contain a single 'cleanly defined' hydraulic jump and consequently sets a standard for later analysis. Section 3.3 is from $x = 3$ to 12 where a jump may also occur.

Additional measurements in the Samoan Passage are described by Voet *et al.* (2015, 2016).

3.2. *The tow-yo section from 19 to 25 km*

Profiles of potential density and northwards velocity at 1 km spacing in the section of increasing depths from $x = 19$ to $x = 25$ are shown in figures 4(*a*) and 4(*b*), respectively. Table 1 shows the results of fitting the η profiles to these data as

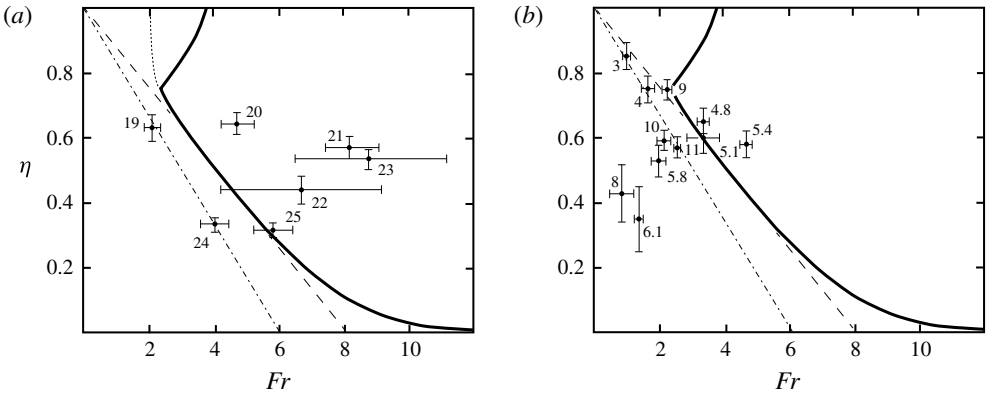

FIGURE 5. Values of η and Fr at numbered kilometre locations in the Samoan Passage (*a*) $x = 19$–25 and (*b*) $x = 3$–12. Points to the right of the bold line are supercritical, those to the left subcritical. The uncertainties in observed values of η and Fr are shown by error bars. The dot-dashed line corresponds to an interfacial gradient Richardson number of 1/3.

Location x (km)	Depth (m)	h (m)	η	Ri	Fr	Super/sub-critical
19	5022	537	0.64 ± 0.04	0.35	2.1 ± 0.2	Sub
20	5006	426	0.64 ± 0.03	0.15	4.7 ± 0.5	Super
21	5038	383	0.57 ± 0.03	0.11	8.0 ± 0.8	Super
22	5092	432–617	0.44 ± 0.04	0.17 ± 0.13	6.7 ± 2.5	Uncertain
23	5140	520 ± 45	0.54 ± 0.03	0.11 ± 0.10	8.7 ± 2.4	Super
24	5076	561	0.33 ± 0.02	0.33	4.1 ± 0.4	Sub
25	5111	521	0.31 ± 0.02	0.24	5.7 ± 0.6	Uncertain

TABLE 1. Values derived from fitting η profiles to data at locations of $x = 19$ to 25 in the Samoan Passage. The possible errors in the estimates of η and Fr (and of h and Ri at $x = 22$ and 23) are indicated by '$\pm$' or a range of values. Locations where the range of possible values crosses the subcritical–supercritical boundary are labelled 'uncertain'.

described in appendix A. Here η (with no subscript) is derived from the best fit of an η profile to the observations at a position, x. The mean thickness, ηh, of the lower layer is 256 m and its mean northward speed is 0.43 m s^{-1}. The mean thickness of the interfacial layer is 274 m. With the estimated values of Fr and η, figure 2 (with $\eta_1 = \eta$) is used to determine whether or not the flow at various positions, x, can support a hydraulic jump. Points in the (Fr, η) plane denoted by their position, x, are shown in figure 5(*a*), which is divided as in figure 2. At $x = 19$, the Froude number, $Fr = 2.1$ and $\eta = 0.64$, and (from figure 2*b*) the flow is subcritical (i.e. no hydraulic jump is possible). At $x = 20$, $Fr = 4.7$ and $\eta = 0.64$ and, as shown by the location of the point in figure 5(*a*), according to the model the flow is supercritical with (figure 2*b*) a single solution for the downstream flow. The density profile contains few regions of static instability and there is a relatively low dissipation rate (figure 3).

Figure 6 (reproduced from TL's figure 5) shows contours of various downstream quantities derived from the model corresponding to upstream values, η_1 and Fr. The predicted downstream values (at a location where $Ri \sim 1/3$) that correspond to

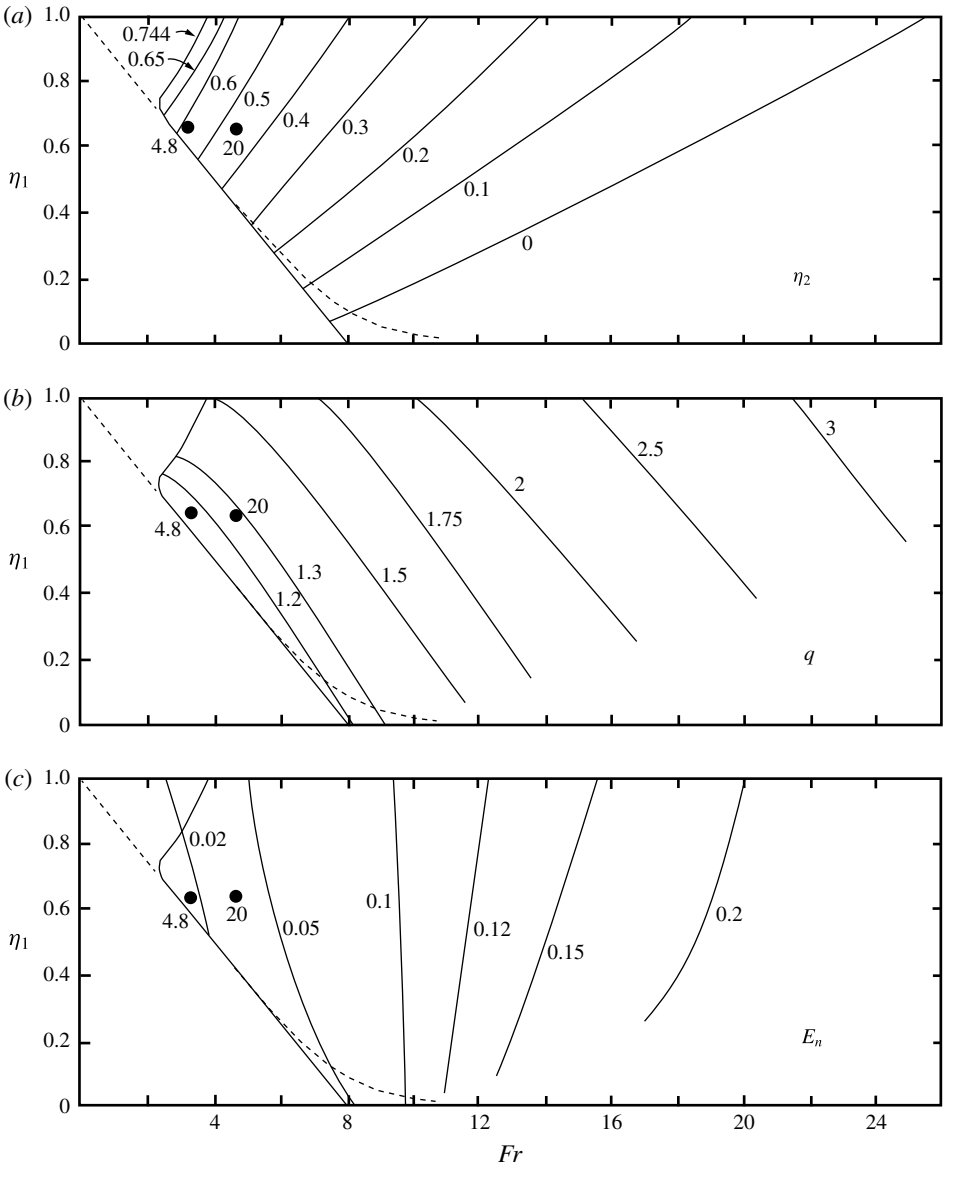

FIGURE 6. The model's predictions of (*a*) the downstream profile parameter, η_2, (*b*) the ratio of flowing layer thickness, $q = h_2/h_1$, and (*c*) the non-dimensional energy loss, E_n, in the (η_1, Fr) plane. Values of (upstream) η_1 and Fr are indicated at labelled locations, $x = 4.8$ and 20 in the Samoan Passage where, according to the model, the flow becomes supercritical.

upstream values η_1 and Fr at $x = 20$ are $\eta_2 = 0.47$ (figure 6*a*) and $q = h_2/h_1 = 1.29$ (figure 6*b*). The latter has $q > 1$ and implies that the thickness of the overall flowing layer at the downstream location should exceed that upstream or, since at $x = 20$ the layer thickness is $h_1 = 426$ m (table 1), the predicted downstream value is $h_2 = 549$ m. Moreover, the predicted downstream thickness of the lower layer, $\eta_2 h_2$, is 258 m, i.e. the thickness of the uniform layer below the interfacial layer should be less than that

upstream, $\eta_1 h_1 = 271$ m. Since the upper edge of the interfacial layer is predicted to increase in height above the bottom and the lower edge to decrease, a mode 2 transition from upstream to downstream of the transition is expected as noted in § 2. But, to comply with the model, does the flow attain an approximately steady subcritical state with $Ri_2 \approx 1/3$ at some $x > 20$?

Although there is a well-defined shear and density interface between 4670 and 4790 m depth at $x = 21$, above it the density profile has a large region of static instability with variable shear at depths of 4530–4700 m, marked 'A' in figure 4(*a*), and this x location (the parameters of the interfacial region also implying in figure 5(*a*) that the flow is supercritical) is presumably within a hydraulic jump downstream of $x = 20$ following its supercritical state. At $x = 22$ there is a near-uniform layer from 4520 to 4750 m, marked 'B' in figure 4(*a*), containing a 60 m high region of static instability. At $x = 23$, there is what appears to be an 80 m deep layer of residual overturn, marked 'C', near 4650 m. Evidence of this mixing region persists at $x = 24$, marked 'D'. The presence of the inversions (statically unstable regions) is reflected by the large uncertainty in Fr shown in table 1 and figure 5(*a*) at $x = 22$ and 23, and consequently the sub- or supercritical state of the flow is not definitely known at $x = 22$, although the latter is favoured. However, at $x = 24$ the flow becomes subcritical (although the interfaces in both density and velocity are somewhat irregular, possibly layered) with $Ri = 0.33$ ($\approx 1/3$) and a Froude number that approaches the dot-dashed line in figure 2(*c*), reproduced in figure 5(*a*), as required in the model flow downstream of KHI.

The features of the jump described in the last paragraph are illustrated in more detail in the potential density contours of figure 7. The mixing region is outlined by an oval-shaped curve to indicate its location and approximate dimensions. It is characterized by relatively uniform density but with frequent inversions. It begins near $x = 20$, the position where the flow is first predicted to be supercritical. The mixing region appears initially near 4600 m depth, approximately 410 m off the bottom, splitting into two the upstream stratified interfacial layer between 4530 and 4650 m. The potential density of the fluid where the mixed layer first appears is slightly less than the mean potential density in this interfacial layer. At $x = 22$ the layer develops into a vertically near-uniform region containing frequent density inversions extending from 4480 to 4770 m depth. At $x = 23$, the centre of the mixing region is at 4650 m, approximately 485 m off the bottom. The density of the oval-shaped mixing region increases with x as more dense water is entrained from the bottom layer. Overall the layer of mixing resembles a mid-water (i.e. separated by approximately 200 m from the bottom) 3.7 km long rotor-like structure following the gradual bottom slope, although no significant sustained flow in the upstream direction was recorded that might confirm the circulatory flow of a rotor. At its maximum the mixing layer is approximately 390 m in height, and its aspect ratio – height divided by length – is approximately 0.08. The velocity field is more uncertain and less firmly structured than the density, but the oval layer appears to have a generally weak flow above its stratified base below which the near-bed northerly flow continues at approximately 0.4 m s^{-1}. The mixing layer forming the hydraulic jump has a form reminiscent of a steady spilling surface-wave breaker (e.g. Rapp & Melville (1990)), like that downstream of a weir led by a 'toe' near $x = 20$, $z = 4600$ m. There is no evidence that it is initiated by an overturn caused by convective instability (as in a plunging surface-wave breaker) or by KH billows, characterized, for example, by 'braids', high-gradient regions between periodic billows, although the uniformity of the layer is sustained by static instability and convection. Its form is similar to that produced

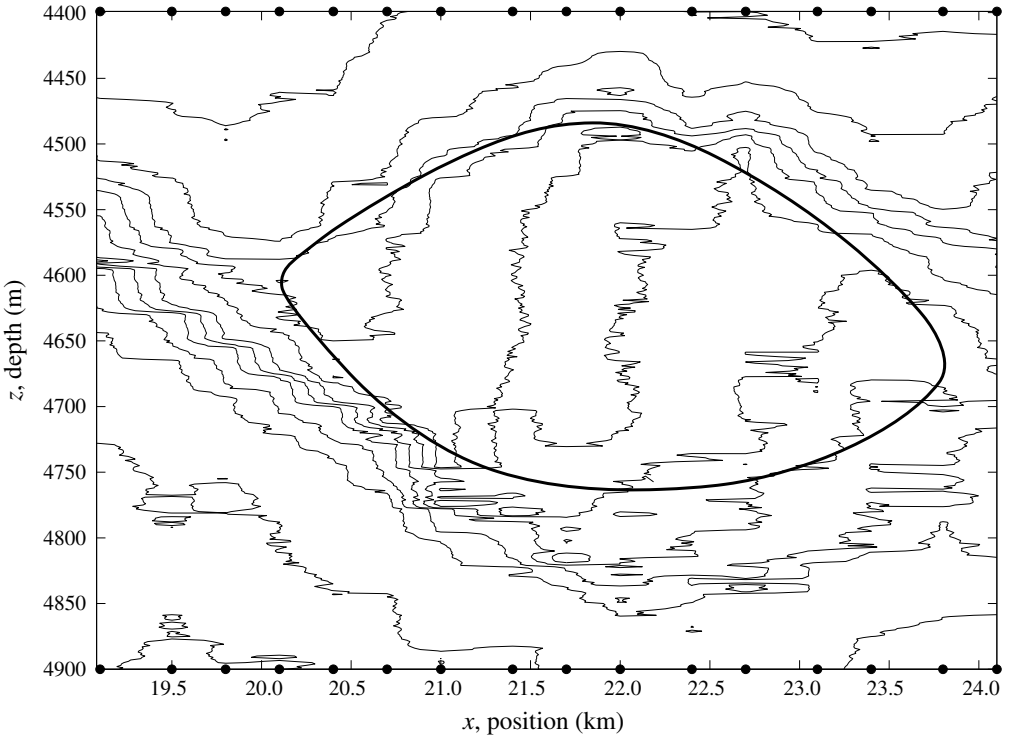

FIGURE 7. Contours of potential density at intervals of 5×10^{-3} kg m^{-3} between $x = 19.1$ and $x = 24.1$ and depths ranging from 4400 to 4900 m in the Samoan Passage. The mean horizontal locations of vertical profiles made by the tow-yo are indicated by dots on the x-axis. The flow becomes supercritical at $x \approx 20$. The approximate position of the mixing region associated with the hydraulic jump is indicated by the oval-shaped curve. The step-like structure of the unsmoothed contours sloping downwards from $x = 19.1$, $z = 4680$ m is probably unreal, a consequence of interpolation by the computer package used to construct the contours as a narrow density interface moves downwards as x increases.

by breaking forced internal waves in the atmosphere above mountain ridges, modelled by Afanasyev & Peltier (1998, see especially their figure 12*d*) and by Yakovenko, Thomas & Castro (2011).

The values of η and h at $x = 24$ are 0.33 and 561 m, respectively, compared to the model's predicted values of 0.47 and 549 m, respectively, for a jump produced by the flow at $x = 20$. The lower layer thickness at $x = 24$ is 186 m, less than the predicted 258 m, but at least showing that the transition is of mode 2, as predicted. In view of the assumptions made in the theoretical model, of the uncertainty in fitting the η profiles to data (reflected in the error bars of figure 5*a*), of whether the profiles at $x = 20$ represent the flow conditions immediately before the transition, and of the unaccounted-for variations in bottom topography shown in figure 3 over the horizontal extent of the transition layer shown in figure 7, it is not surprising that the predicted values differ somewhat from the observed. The density within the interfacial layer is irregular and 'step-like' at $x = 25$ (figure 4*a*). At this location, however, the northward velocity of the flow above the interfacial layer is approximately 0.1 m s^{-1}, violating the model's assumption of zero flow.

Contours of a non-dimensional energy loss in the jump, E_n, in (Fr, η_1) space, estimated by TL (their equation (4.3)), are given by figure 6(*c*). The value of E_n is related to the mean rate of dissipation of turbulent kinetic energy per unit mass in the hydraulic jump, ε, by

$$\varepsilon = E_n U_1^3 (1 + 3\eta_1)/\{4L_j[(1 - \eta_1) + q(1 - \eta_2)]\}, \tag{3.1}$$

where L_j is the horizontal extent of the transition region associated with the hydraulic jump, $q = h_2/h_1$, and U_1 (≈ 0.43 m s^{-1}) is the speed of the lower layer upstream of the jump. Using the upstream values of η_1 and Fr at $x = 20$, figure 6(*c*) gives $E_n \approx 0.035$. Selecting the downstream value of η_2 as that at $x = 24$, and choosing $L_j = 4$ km (the separation distance between the upstream and downstream locations) gives a mean value, $\varepsilon = 4.1 \times 10^{-7}$ W kg^{-1}. This is comparable to the values observed and given in Alford *et al.*'s figures 2 and 3(*c*), the latter reproduced here in figure 3. A further comparison of theory and data is made in appendix D: the approximate time required for turbulence to collapse is consistent with the observations of the length of the active mixing region estimated to be approximately $6U_1N^{-1}$, where N is the mean buoyancy frequency of the stratified region surrounding the upstream interfacial layer.

In summary, a transition begins at $x = 20$, the location where, according to the model, the flow becomes supercritical, and it takes the form of an elongated mixing layer. If this is a rotor, it is similar to those found in numerical studies of moving bores by Ogden & Helfich (2016). It is separated from the seabed by a relatively strong downslope bottom flow, and thus differs from the near-boundary rotors found in large internal waves in the lee of mountains described by Scorer (1955, 1972, e.g. his 1972 figure 5.7i) and Doyle & Durran (2007). No KH billows or braids are apparent in the tow-yo profiles immediately downstream of $x = 20$.

3.3. *The tow-yo section from 3 to 12 km*

Table 2 and figure 5(*b*) show the results of fitting the η profiles to data in $3 \leqslant x \leqslant 12$. The mean thicknesses, the averages of ηh and h of the other flowing layers between $x = 3$ and $x = 12$, are 283 and 484 m, respectively, and the mean northward speed of the dense lower layer is 0.30 m s^{-1}. However, at $x = 7$, the flow is unusually small, less than 0.05 m s^{-1}, throughout the depth range sampled by the tow-yo. Although the density profile was 'normal', with a well-defined interfacial layer between depths of approximately 4300 and 4700 m, no northward-going lower layer appears in the velocity profile. We have no simple explanation for this and it was not possible to fit consistent η profiles to both velocity and density.

According to the model the flow becomes supercritical at $x = 4.8$, returning to subcritical at $x = 5.8$. As shown in the contours of potential density in figure 8 a 100 m high structure with numerous density inversions outlined by the oval-shaped curve appears in the flow at $x = 4.8$. Its density is approximately equal to the mean of that in the upstream interfacial layer and it divides this layer into two. This mixing region extends approximately 1 km downstream, ending at $x \approx 5.8$, the location at which the flow returns to a subcritical state. The aspect ratio of the mixing region is approximately 0.1 compared with 0.08 for the transition at $x = 20$ shown in figure 7. Its length as predicted in appendix D is $6U_1N^{-1} \approx 1.5$ km rather than the 1 km observed. Other mixing layers appear beyond $x = 5.8$, e.g. near $x = 6.1$, $z = 4680$ m, where, according to the model, the flow is subcritical but downstream of substantial increases in water depth.

Location (km)	Depth (m)	h (m)	η	Ri	Fr	Super/sub-critical
3	4776	458	0.85 ± 0.04	0.30	0.98 ± 0.1	Sub
4	4706	344	0.75 ± 0.04	0.31	1.6 ± 0.2	Sub
4.2	4706	291	0.74 ± 0.04	0.31	1.7 ± 0.2	Sub
4.5	4753	338	0.72 ± 0.04	0.32	1.8 ± 0.2	Sub
4.8	4756	356	0.65 ± 0.04	0.22	3.3 ± 0.2	Super
5.1	4803	378	0.60 ± 0.05	0.24	3.3 ± 0.5	Uncertain
5.4	4805	355	0.58 ± 0.04	0.18	4.6 ± 0.2	Super
5.8	4889	409	0.53 ± 0.05	0.48	1.9 ± 0.2	Sub
6.1	4888	538	0.35 ± 0.1	1.0	1.3 ± 0.07	Sub
7	4952	*				
8	4936	596	0.43 ± 0.09	1.5	0.78 ± 0.33	Sub
9	4856	431	0.75 ± 0.03	0.20	2.2 ± 0.05	Uncertain
10	4904	454	0.59 ± 0.03	0.39	2.1 ± 0.2	Sub
11	4920	470	0.57 ± 0.03	0.33	2.5 ± 0.04	Sub
12	4952	562	0.57 ± 0.04	0.45	1.9 ± 0.2	Sub

TABLE 2. Values derived from fitting η profiles to data at locations of $x = 3$ to 12 in the Samoan Passage. The uncertainty in the estimates of η and Fr are indicated by '±'. At $x = 7$ (marked $*$), the flow is small, less than 0.1 m s^{-1}, perhaps being blocked, and it was not possible to fit consistent η profiles to both velocity and density. At $x = 9$ the flow is marginal (i.e. on or very close to the supercritical–subcritical boundary in figure 4*b*) although unstable to KHI.

Using the values of η and Fr at $x = 4.8$ as those upstream of a transition, figure 6(*a*) predicts $\eta_2 \approx 0.57$ downstream. This compares fairly well with the observed value, 0.53, at the subcritical downstream end of the mixed structure at $x = 5.8$. The Richardson number at $x = 5.8$ is, however, 0.48, indicating a stable flow, but greater than the value, $Ri_2 = 0.33$, adopted in the model. The value of E_n determined from figure 6(*c*) at $x = 4.8$ is approximately 0.018. The mean value of ε in the 1 km between $x = 4.8$ and 5.8 derived using (3.1) is approximately 1.0×10^{-6} W kg^{-1}, in order-of-magnitude accord with the values shown in figure 3. Although smaller than the feature associated with the hydraulic jump at $x = 20$, the mixed structure shares many of its general characteristics, including its being separated from the seabed by the near-bottom northerly flow of dense water and by an absence of any clear evidence of KH billows or braids.

4. The Red Sea Outflow

A different Froude number, described as a 'bulk Froude number' and denoted here by Fr_P, is used by Peters *et al.* (2005) in the analysis of data from the Red Sea Outflow in the Gulf of Aden, a near-bottom flow with velocity and density structure similar to the profiles considered in the Samoan Passage. In terms of the notation of § 2, Peters *et al.* define Fr_P 'following discussion with Price 2003 (personal communication)' by

$$\begin{aligned} Fr_P^2 &= (U_1/2)^2/\{g\Delta[\eta_1 h_1 + h_1(1-\eta_1)/2]\}, \\ &= U_1^2/[2g\Delta h_1(1+\eta_1)], \end{aligned} \tag{4.1}$$

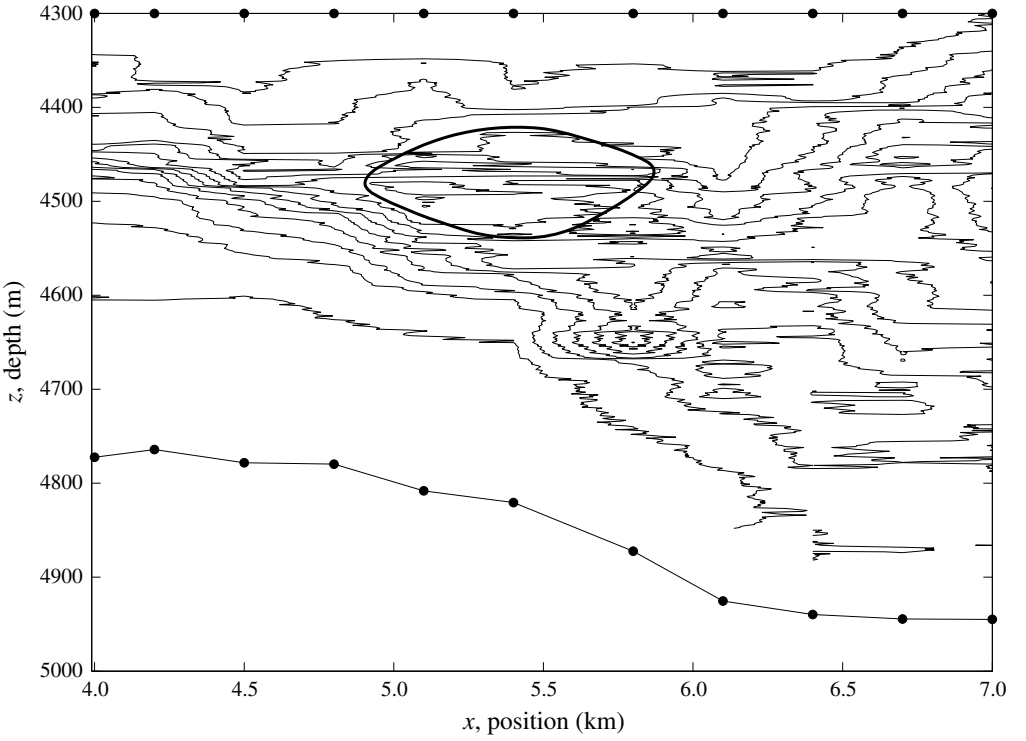

FIGURE 8. Contours of potential density at intervals of 5×10^{-3} kg m^{-3} through the hydraulic jump between $x = 4$ and $x = 7$ below 4300 m depth in the Samoan Passage. The mean horizontal locations of vertical profiles made by the tow-yo and the depth of the seabed are indicated by the dots. Tow-yo profiles extend only to approximately 40 m from the seabed so no data are available closer to the seabed. The flow becomes supercritical at $x \approx 4.8$. The approximate position of the oval-shaped mixing region associated with the hydraulic jump is outlined.

or, in terms of Fr given by (2.5) and the local value, η_1,

$$Fr_P^2 = Fr/[2(1 + \eta_1)]. \tag{4.2}$$

The critical curves in the (η_1, Fr) plane shown in figure 2 are translated to the (η_1, Fr_P) plane in figure 9. The thick line represents the lowest values of Fr_P at which, according to the model described in § 2, a hydraulic transition can occur for given η_1; values of the minimum Fr_P vary with η_1. The smallest Fr_P at which transition can occur is 0.80 at $\eta_1 = 0.74$. The minimum (or critical) Fr_P is equal to unity only when $\eta_1 = 0.6$.

The Red Sea Outflow exits the Red Sea through the Strait of Bab el Mandeb and passes down two channels in the Gulf of Aden between 12° N and 12°30′ N, the northern and southern channels denoted by Peters *et al.* (2005) as NC and SC, respectively. The outflow, confined to the channels, is conceived by Peters & Johns (2005) and Peters *et al.* (2005) in terms of gradually entraining plumes of dense water rather than gravity currents and in which the spread is dominated by localized hydraulic jumps. Measurements are made using a package combining an LADCP and CTD. During the period of stronger flow in observations made in winter, values of Fr_P

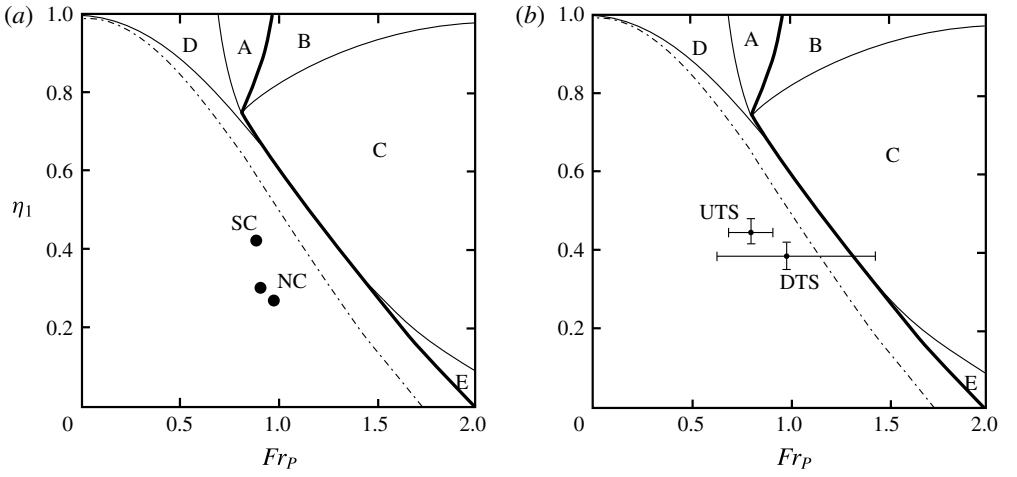

FIGURE 9. The critical curves of figure 2 translated to the (η_1, Fr_P) plane. Regions A–E correspond to those in figure 2(*b*,*c*). The thick line represents the lowest values of Fr_P at which a hydraulic transition can occur for given η_1. In (*a*) points are taken from Peters & Johns (2005) in the two channels, NC and SC, of the Red Sea Outflow. In (*b*) points are taken from Gasser *et al.* (2011) and Nash *et al.* (2012) at stations UTS and DTS in the Mediterranean Outflow. The dot-dashed line corresponds to an interfacial gradient Richardson number of 1/3.

estimated by Peters & Johns (2005) have locally maximum values of approximately 0.93 and 0.97 at down-channel distances in the NC of approximately 70 and 120 km, respectively, from the Strait of Bab al Mandeb, and 0.88 at approximately 60 km in the SC. At all three locations, the rate of dissipation of turbulent kinetic energy, estimated using an assumed proportionality between the Ozmidov and Thorpe length scales, is also maximal, suggesting the possible presence of hydraulic jumps. At these locations the value η_1, taken here as the ratio of the bottom layer to the total thickness of the flowing layer (H_b/H_p in the notation of Peters & Johns (2005)) is approximately 0.30 and 0.27 in the NC, and 0.42 in the SC. The corresponding points in the (Fr_P, η_1) plane are shown in figure 9(*a*) and indicate that, although the values of Fr_P exceed the minimum for hydraulic jumps to occur, the flows should be subcritical, stable to hydraulic jumps at the estimated η_1. Values are, however, uncertain. Peters & Johns (2005) and Peters *et al.* (2005) take the depth of the lower layer (ηh, or H_b in their notation) as the height above the seabed at which the downstream velocity is a maximum, less than the estimate of $\eta_1 h$ determined as in appendix A. The total thickness of the flowing layer (H_p in their notation) is taken in a less precise way, depending on the speed or direction of the velocity, or on the salinity. The value $\eta_1 = H_b/H_p$ is likely to be less than that found in appendix A, and Fr_P may consequently be overestimated. There is no clear evidence from observations or theory of the presence of hydraulic jumps in the Red Sea Outflow. Rather, the spreading of the outflow down the channels in the Gulf of Aden appears to be dominated by a more gradual process of turbulent entrainment as concluded by the two sets of authors.

5. The Mediterranean Outflow

Gasser *et al.* (2011) and Nash *et al.* (2012) report observations using moorings and tow-yos in the Mediterranean Outflow in the Gulf of Cadiz 70 km west of the Strait of Gibraltar and to the west of the Espartel Sill, the most western sill of the Strait. At this location the dense outflow is confined to a westward-flowing layer of water, some 150 m thick and of relatively high salinity, moving westward over the seabed at approximately 1.2 m s^{-1}. Profiles of density and velocity are derived from the surface to the bottom with 1 km horizontal resolution. Flow in the layer overlying the outflow is of order 0.2 m s^{-1} to the east. Gasser *et al.* (2011) show roughly 10 km long downstream tow-yo sections of salinity, downstream velocity and gradient Richardson number at four stages of the M_2 tidal cycle. Nash *et al.* (2012) present a tow-yo section of downstream velocity and $\log \varepsilon$ at the same time as that of the low tidal flow section presented by Gasser *et al.*, and focus attention on two stations in the section, separated by approximately 3.5 km, UTS (upstream at 6°19.23′ W, 35°47.04′ N, where the water depth is approximately 417 m) and DTS (downstream at 6°21.00′ W, 35°46.51′N, in 454 m).

Following Peters *et al.* (2005), Nash *et al.* (2012) use the bulk Froude number, Fr_P, in their analysis, but assume, without formal justification, that transition occurs at $Fr_P = 1$. At UTS, 90 % of the estimates of Fr_P lie between 0.70 and 0.92 (with a mean of 0.81). The mean dissipation, ε, in the outflowing layer is approximately 1×10^{-6} W kg^{-1}. The value of η estimated from the profiles given by Gasser *et al.* (2011) and Nash *et al.* (2012) is 0.45 ± 0.03. Respective points are shown in figure 9(*b*). They indicate that, according to the model, the flow is subcritical and stable to a hydraulic transition at UTS.

Approximately 1–2 km west of UTS Nash *et al.* (2012, their figure 3*b*,*c*) find a notable increase in the high-frequency displacement of isopycnals, an increase in interface thickness and a rise in ε to a mean value of approximately 1×10^{-5} W kg^{-1} in the outflow, suggesting that a mode 2 transition has occurred. Further downstream at DTS the mean $Fr_P = 0.99$ and 90 % of the estimates of Fr_P lie between 0.63 and 1.45, 45 % having $Fr_P > 1$, and η is equal to 0.39 ± 0.03. As shown in figure 9(*b*), the upper values of these estimates of Fr_P and η imply that a hydraulic jump is possible. It is likely, however, that conditions for a jump have been reached upstream of DTS and that DTS lies within the transitional region, this accounting for the relatively large variations in isopycnal depths and in Fr_P or Fr. Similarly large variations in Fr are observed downstream of the hydraulic jump at $x = 20$–21 in the Samoan Passage (figure 5*a*). (Taking the upper values at DTS, $Fr_P \approx 1.45$ and $\eta \approx 0.4$, we find $Fr = 5.85$ from (4.2) while figure 6 gives $\eta_2 \approx 0.3$, $q \approx 0.8$ and $E_n \approx 0.05$. Taking L_j equal to the distance between the two stations, i.e. 3.5 km, and using (3.1), gives $\varepsilon \approx 1.2 \times 10^{-5}$ W kg^{-1}, consistent with the observed dissipation rate at DTS.) Nash *et al.* (2012) use the Taylor–Goldstein equation to examine the stability of the flow at DTS to KHI. The gradient Richardson number of the flow near the centre of the interface above the flowing layer is less than 1/4, and the flow is found to be unstable to KHI, consistent with the larger values of Fr_P being in region C of figure 9(*b*). Downstream (to the west) of DTS the depth of the seabed increases sharply to approximately 500 m, resulting in an increase of η to approximately 0.5, a flow that exhibits 30–50 m overturns and ε exceeding 10^{-5} W kg^{-1}, again suggestive of a hydraulic jump.

6. Discussion

The η profiles defined by (2.2) provide an approximate, if imperfect, description of the continuous profiles of density and velocity found in near-bottom flows through the channels of the Samoan Passage and the outflows from the Red Sea and the Mediterranean. The predictions of the model described in § 2 are used to determine whether flows observed in these three regions are sub- or supercritical to stationary hydraulic transitions.

The majority of selected examples, including those in which hydraulic transitions are suspected in the Red Sea Outflow because of high values of turbulent dissipation (§ 4), appear to be subcritical within the uncertainty of the estimated η and Fr or Fr_P. (High turbulent dissipation may be caused by the stress generated by the rapid flow over a possibly rough seabed, a factor not accounted for in the model.) Downstream of two locations in the Samoan Passage ($x = 20$ and 4.8; figures 5*a* and 5*b*, respectively), the flow appears to have undergone a transition, and the consequent changes appear to be reasonably in accord with the model's predictions, including that of the dissipation of turbulent kinetic energy. The transition is manifest as a downstream-elongated mid-water actively mixing region. Its form downstream of the position at which flow becomes supercritical is most clearly seen in the potential density field of figure 7. A likely hydraulic jump is identified in the Mediterranean Outflow between Nash *et al.*'s (2012) stations UTS and DTS (§ 5) but none in the Red Sea Outflow in the Gulf of Aden, in accord with analysis by Peters & Johns (2005) and Peters *et al.* (2005) (§ 4).

Further to the discussion in § 2, it is of note that only in the possibly rare cases where η is small and Fr large (region E in figure 2*c*) does the model predict that internal hydraulic jumps occur but not KHI. One case (at $x = 9$ in the Samoan Passage, figure 5*b* and table 2) is found, however, in which the flow is unstable to KHI but apparently not liable to a hydraulic transition (i.e. regions A or D in figure 2*b*).

There is a further possibility not accounted for in the model: that the features identified from the tow-yo data as hydraulic jumps or KHI are not stationary, but are propagating downslope as internal roll waves similar to those reported by Fer, Lemmin & Thorpe (2002). This is, however, unlikely, as later observations in the Samoan Passage analysed by G. Voet have found very similar jump structures in the same locations. For example, figure 10 shows the hydraulic jump near $x = 20$ surveyed about two years after that shown in figure 7. The overall structure outlined by the oval curve remains generally the same, with comparable height and length but with an aspect ratio of approximately 0.06. The mixing layer splits the upstream interfacial layer into two, and the mean density in the layer increases with x, although less rapidly in figure 10 than in figure 7. The depth of the toe in figure 10 is approximately 100 m deeper than in figure 7 and it is approximately 500 m further downstream. Although Yakovenko *et al.* (2011) draw attention to the long-period vacillation of lee wave systems and mixing near a topographic feature, there is no evidence here of such variability, only that the feature persists. The theory of Rottman, Broutman & Grimshaw (1996) supporting variability finds that it is mainly due to internal waves that persist near the topography, but occasionally propagate upstream, a feature excluded in the present hydraulic jump model.

The Earth's rotation is disregarded in the model. Its effect on the hydraulic jumps illustrated in figures 7 and 8 may be assessed by the magnitude of a Burger number, Bu. This is equal to the ratio of the internal Rossby radius of deformation, NH/f, divided by the extent of the mixing region, L_j, where N is the mean buoyancy frequency of the fluid in which the jump occurs, H is the thickness of the mixing

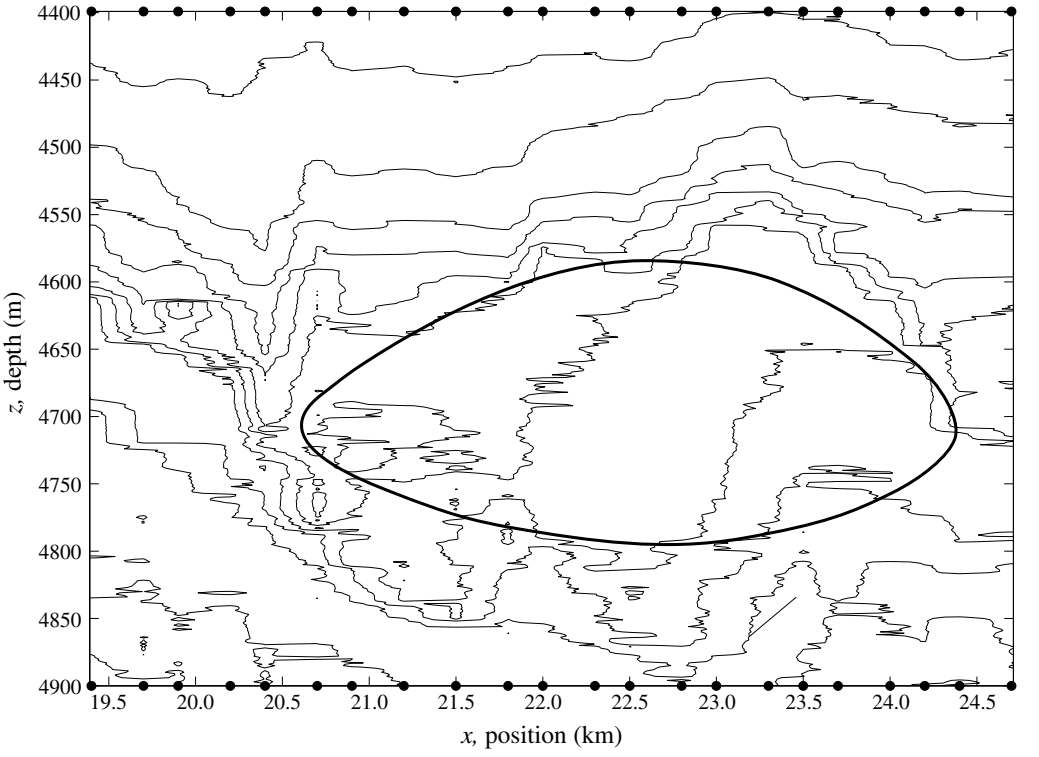

FIGURE 10. Contours of potential density at intervals of 5×10^{-3} kg m^{-3} through the hydraulic jump between $x = 19.4$ and $x = 24.7$ and in depths ranging from 4400 to 4900 m in the Samoan Passage obtained approximately two years later than those of the jump shown in figure 7. The mean horizontal locations of vertical profiles made by the tow-yo are indicated by dots on the x-axis. The approximate position of the mixing region associated with the hydraulic jump is indicated by the oval-shaped curve.

layer produced by the jump, and f is the Coriolis frequency, 2.03×10^{-5} s^{-1}, at the latitude of the Samoan Passage. Estimated values of Bu are 3.1 ± 1.4 and 4.2 ± 0.3 for the jumps at $x = 20$ and 4.8, respectively. These values exceed unity and indicate that here in the Samoan Passage, although not necessarily in the Red Sea or Mediterranean Outflows, rotation has a relatively unimportant effect in the region downstream of a transition.

7. Conclusions

Available observations are largely consistent with the predictions of the model sketched in figure 1 and summarized in figure 2. The prediction of hydraulic transitions might, however, be refined and more closely tested by selecting a model with, instead of η profiles, velocity and density profiles that better match those observed, as in Thorpe (2010). The transition downstream of $x = 20$ in the Samoan Passage provides a well-defined example of a hydraulic jump in the deep ocean and of the consequent changes in density (figure 4). The jump appears to be persistent and possibly quasi-steady, being found in observations made two years apart (figures 7 and 10). It takes the form of a large, near-uniform, mixing layer that splits the

upstream interfacial layer overlying the deep dense layer of flowing water. This mixing region commences at a 'toe' (like that of a spilling surface-wave breaker) at which neither KHI nor convective instability is evident although static and convective instability are present within the mixed layer itself. The mixed layer produced by the transition is similar in form to those ascribed to the breaking of internal waves in the lee of mountain ridges in the atmosphere.

It is likely that a variety of types of hydraulic transitions are possible in stratified shear flows. A similar 'nearly stagnant isolating layer', some 50 m thick and preceded by flow bifurcation, is observed in the relatively shallow water flow over the sill in the Knight Inlet, British Columbia (Farmer & Armi 1999; Winters & Armi 2014; Jagannathan, Winters & Armi 2017). The formation of a near-uniform layer therefore appears to be a characteristic of at least some internal hydraulic jumps. Gasser *et al.* (2011) provide one example of changes in the Mediterranean Outflow downstream of their station UTS occasioned at one phase of the tidal cycle by the presence of 50 m high and 1 km long KH billows. Billows have an important role in the atmospheric jump in the lee of the US Sierra Nevada mountain range (Armi & Mayr 2011). More detailed observations are desirable to provide further examples of hydraulic jumps that might allow their classification, particularly where, according to the model, both KHI and hydraulic jumps are possible as described in § 2.

Acknowledgements

We acknowledge and salute the effort required to collect and analyse the data referred to in this study, particularly by those whose contribution is recognized by Alford *et al.* (2013). Data from the Samoan Passage were collected under National Science Foundation Grants OCE-1029268 and OCE-1029483. The help of Mrs K. Davis in the preparation of figures is gratefully acknowledged.

Appendix A. Fitting model to data

Data from the Samoan Passage used for analysis are listed profiles of the northward component of velocity and the potential density referenced to 4000 m at 1 m vertical intervals obtained by tow-yos. Examples at approximately 1 km horizontal separations are shown in figure 4. The interfacial layer in the velocity profiles is generally more clearly defined than that of the density. (The suffixes, i, in η_i etc. are presently dropped, making no assumptions about whether locations are upstream or downstream of a jump.) At a chosen location (in km) a line is fitted to the velocity profile to represent the velocity interface. This intersects zero velocity at a determined height $z = h$ above the seabed. The mean velocity, U, below the interface generally shows evidence of a frictional bottom boundary layer but is simply fitted by a line, $U = \text{const.}$, meeting the constant gradient line at $z = \eta h$, so defining a value of η and the velocity η profile. The velocity gradient is $U/[h(1-\eta)]$. The difference in densities, $2\Delta\rho_0$, at level ηh and at level h is used to find the density gradient $2\Delta\rho_0/[h(1-\eta)]$. The gradient Richardson number in the interfacial layer ($\eta h < z < h$) is $Ri = 2g\Delta h(1-\eta)/U^2$, and represents and approximately preserves the minimum Richardson number of the observed flow. The Froude number of the upstream flow is $Fr = U^2/(g\Delta h) = 2(1-\eta)/Ri$.

The maximum potential density of the lower layer in this section from the Samoan Passage (at least at 40 m above the seabed, the lower limit of the tow-yo cycles) remains fairly constant, showing that the water at this level is not mixed with the overlying less dense water. (This implies that the parameter δ appearing in TL is

unity.) The speed of the lower layer, however, changes as a consequence of its expansion or contraction as it passes downstream.

Values of η and Fr at numbered x locations in Alford *et al.*'s (2013) data are shown in tables 2 and 1 and figures 5 and 6.

Appendix B. Assumptions of the theory

The hydraulic jump theory (§ 2 and TL) makes a number of assumptions about the real flow that are only approximately satisfied. It is assumed in the model that the velocity upstream and downstream of the stationary hydraulic jump or transition is uniform in a horizontal direction and depends only on the vertical coordinate, z. In reality, the seabed generally slopes (in the Samoan Passage, descending from a depth of approximately 4706 m at $x = 4$ to 5128 m at $x = 25$, a mean gradient of 1.15°, but crossing notable sills at $x = 4$ and 19 and a trough at $x = 7$ in addition to smaller-scale undulations; see figure 3). The real flow is consequently not steady, as assumed, but tends to accelerate downslope, subject to the balance between the downslope component of gravity and the bottom and interfacial drag. It will also respond to changes in channel width and to the tides (although in the Samoan Passage these are relatively weak, less than 0.05 m s^{-1}). Since at the latitude of the Samoan Passage, 8° S, the inertial period is approximately 86 h and the time required to complete the tow-yo section of figures 4 or 7 made at 0.25 m s^{-1} is less than 6 h, inertial oscillations (which have moderate amplitude, typically less than 0.15 m s^{-1}) will contribute little to the changes that are apparent in this section. The model's velocity and density profiles are supposed similar in shape, and the velocity is zero above the interfacial layer. In reality, changes in the flow occur continually both inside and outside the transition region. The density and velocity profiles are similar in that they generally contain an interfacial region of high gradient at the same depths, but (i) the flow above the shear layer is not precisely zero, although generally relatively small (an exception being at $x = 25$ in the Samoan Passage), and (ii) the potential density in the region above the shear layer is not constant but generally has a negative (i.e. statically stable) gradient. This may be sufficiently small to prevent the upward radiation of internal waves (see appendix C). The effects of stationary (possibly breaking; Yakovenko, Thomas & Castro 2014) lee waves generated by the flow over the sill are not taken into account and the transition is not allowed to be undular in form. In the model it is assumed that turbulence in the hydraulic jump collapses to give a Richardson number of approximately 1/3 as observed in laboratory and numerical experiments of KHI. The transition occurs over a level horizontal seabed. In reality, Richardson numbers of approximately 1/3 are found downstream of possible jumps, e.g. at $x = 24$ and at 5.8 and 11 in tables 2 and 1, respectively. Further study is required to extend the simple local model to a broader range of conditions.

Appendix C. Radiation of internal waves

Waves radiating upwards from a hydraulic jump transition region may be forced by KH billows (and other disturbances forced by turbulence) in the hydraulic transition region. The fastest growing KHI disturbances in an η profile move downstream at a speed of approximately $U/2$ and have a wavelength of approximately seven times the interface thickness, $h(1 - \eta)$ (Miles & Howard 1963). Suppose, for generality, that the hydraulic jump contains perturbations of horizontal scale, λ, moving downstream at speed $c \sim U/2$, and that these generate internal waves in an overlying region of

buoyancy frequency, N. If the frequency of the internal waves is σ and their horizontal and vertical wavenumbers are $k = 2\pi/\lambda$ and m, respectively, then $\sigma/k = c$ and

$$\sigma^2 = N^2k^2/(k^2 + m^2), \tag{C 1}$$

the dispersion relation, disregarding the effect of the Coriolis force. This gives $m = \pm k(N^2/\sigma^2 - 1)^{1/2}$, which is real if $N/\sigma = N/ck > 1$. Waves can radiate upwards from the turbulent transition region if m is real or are evanescent, decaying exponentially upwards, if m is imaginary.

With the observed values in the Samoan Passage at x = 3–12 (or 19–25) of $c = U/2 = 0.15$ (or 0.21) m s^{-1}, $N = 4.62 \times 10^{-4}$ (or 4.79×10^{-4}) s^{-1} (greatly exceeding the inertial frequency, approximately 2.03×10^{-5} s^{-1}) and with $k = 2\pi/[7h_1(1 - \eta_1)]$ corresponding to KH billows, we have $k = 4.47 \times 10^{-3}$ (or 3.28×10^{-3}) m^{-1} giving $N/ck = 0.69$ (0.70). These values are less than 1, so that the forced waves are evanescent, trapped near the top of the flowing layer. The billow wavelengths, $\lambda = 7h_1(1 - \eta_1) \sim 1.41$ (1.92) km, are a substantial fraction of, or exceed, the approximate length of transitions, 1.0 km (3.9 km) estimated in § 3.3 (§ 3.2). Only waves with horizontal wavelengths $> 2\pi c/N \sim 2.0$ (or 2.8) km may radiate upwards from the turbulent hydraulic transition, leading to a loss in energy and momentum. (A study of internal waves in the Samoan Passage by Voet finds that waves appear to be trapped in the lower layer and do not radiate much energy beyond the interfacial layer.)

Appendix D. The collapse of turbulence in the hydraulic jump

According to the laboratory experiments of Thorpe (1973), the time for turbulence to collapse following KHI and to reach a state in which $Ri \sim 0.33$ (after which there is little change in layer thickness) is approximately given by $\tau = 6U_1/g\Delta$. (The flow may still continue to contain 'striations', remnants of turbulent overturns, beyond a time $\tau_1 = 12U_1/g\Delta$. The times for the decay of available potential energy in the turbulence or of the evolution of the efficiency parameter, Γ, in the numerical calculations of Smyth *et al.* (2001) are consistent with a time τ_1 rather than the smaller τ.) Supposing that turbulence is advected downstream at a mean speed $U_1/2$, the distance downstream from a jump or 'KHI event' to where the gradient Ri becomes equal to 1/3 is approximately $\tau U_1/2 = 3.5h_1Fr$. Using values at $x = 20$, the distance downstream before the flow evolves to a mean Richardson number of approximately 1/3 is therefore approximately 6 km, somewhat greater than the distance between the observations at $x = 20$ and 24 or over the horizontal extent of the transition event shown in figure 7. The larger time, τ_1, suggests that remnants of the turbulence from a transition near $x = 20$ may be carried to at least 12 km downstream, and the irregular structure remaining in the observed interface at $x = 25$ is evidence that this may be so.

An alternative, again approximate, derivation of a collapse time but better representing that from a statically unstable region, is found from the laboratory study by Lawrie & Dalziel (2011) of the decay of turbulence when an initially statically unstable region spreads into stably stratified surroundings with uniform buoyancy frequency, N. Shear is, however, absent. The decay time is approximately $12N^{-1}$. Taking $N \approx 6.2 \times 10^{-4}$ s^{-1} to represent the stratification in the water surrounding the mixing layer at A–D in figure 4(*a*) gives a decay time of approximately 2×10^4 s or, if water is carried at mean speed $U_1/2 \approx 0.215$ m s^{-1}, a decay distance $6U_1N^{-1}$, of 4.2 km, which is more consistent with that observed.

REFERENCES

AFANASYEV, YA.D. & PELTIER, W. R. 1998 The three-dimensionalization of stratified flows over two-dimensional topography. *J. Atmos. Sci.* **55**, 19–39.

ALFORD, M. H., GIRTON, J. B., VOET, G., CARTER, G. S., MICKETT, B. & KLYMAK, J. M. 2013 Turbulent mixing and hydraulic control of abyssal water in the Samoan Passage. *Geophys. Res. Lett.* **40**, 4668–4674.

ARMI, L. & MAYR, G. T. 2011 The descending stratified flow and hydraulic jump in the lee of the Sierras. *J. Appl. Meteorol. Climatol.* **50**, 1995–2011.

BAINES, P. G. 1995 *Topographic Effects in Stratified Flows*, p. 482. Cambridge University Press.

BAINES, P. G. 2016 Internal hydraulic jumps in two-layer systems. *J. Fluid Mech.* **787**, 1–15.

DOYLE, J. D. & DURRAN, D. R. 2007 Rotor and subrotor dynamics in the lee of three-dimensional terrain. *J. Atmos. Sci.* **64**, 4202–4221.

FARMER, D. M. & ARMI, L. 1999 Stratified flow over topography: the role of small-scale entrainment and mixing in flow establishment. *Proc. R. Soc. Lond.* A **455**, 3221–3258.

FER, I., LEMMIN, U. & THORPE, S. A. 2002 Winter cascading of cold water in Lake Geneva. *J. Geophys. Res.* **107** (C6), doi:10.1029/2001JC000828.

GASSER, M., PELEGI, J. I., NASH, J. D., PETERS, H. & GARCIA-LAFUENTE, J. 2011 Topographic control on the nascent Mediterranean outflow. *Geo.-Mar. Lett.* **31**, 301–314.

JAGANNATHAN, A., WINTERS, K. B. & ARMI, L. 2017 Stability of stratified downslope flows with an overlying stagnant isolating layer. *J. Fluid Mech.* **810**, 392–411.

LAWRIE, A. G. W. & DALZIEL, S. B. 2011 Rayleigh–Taylor instability in an otherwise stable stratification. *J. Fluid Mech.* **688**, 507–527.

MILES, J. N. & HOWARD, L. N. 1963 Note on a heterogeneous shear flow. *J. Fluid Mech.* **20**, 331–336.

NASH, J. D., PETERS, H., KELLY, S. M., PELEGRI, J. L., EMELIANOV, M. & GASSER, M. 2012 Turbulence and high-frequency variability in a deep gravity current outflow. *Geophys. Res. Lett.* **39**, L18611.

OGDEN, K. A. & HELFICH, K. R. 2016 Internal hydraulic jumps in two-layer flows with upstream shear. *J. Fluid Mech.* **789**, 64–92.

PETERS, H. & JOHNS, W. E. 2005 Mixing and entrainment in the Red Sea outflow plume. Part II: turbulence characteristics. *J. Phys. Oceanogr.* **35**, 584–600.

PETERS, H., JOHNS, W. E., BOWER, A. S. & FRATANTONI, D. M. 2005 Mixing and entrainment in the Red Sea outflow plume. Part I: plume structure. *J. Phys. Oceanogr.* **35**, 569–583.

PETTRÉ, P. & ANDRÉ, J.-C. 1991 Surface pressure change through Loewe's phenomena and katabatic flow jumps: study of two cases in Adélie Land, Antarctica. *J. Atmos. Sci.* **48**, 557–571.

POLZIN, K., SPEER, K. G., TOOLE, J. M. & SCHMITT, R. W. 1996 Intense mixing of Antarctic Bottom Water in the equatorial Atlantic Ocean. *Nature* **380**, 54–56.

RAPP, R. J. & MELVILLE, W. K. 1990 Laboratory measurements of deep water breaking waves. *Phil. Trans. R. Soc. Lond.* A **331**, 735–800.

ROTTMAN, J. W., BROUTMAN, D. & GRIMSHAW, R. 1996 Numerical simulations of uniformly stratified fluid flow over topography. *J. Fluid Mech.* **306**, 1–30.

SCORER, R. S. 1955 The theory of airflow over mountains – IV. Separation of flow from the surface. *Q. J. R. Meteorol. Soc.* **81**, 340–350.

SCORER, R. 1972 *Clouds of the World*, p. 176. David & Charles.

SMYTH, W. D., MOUM, J. N. & CALDWELL, D. R. 2001 The efficiency of mixing in turbulent patches: inferences from direct simulations and microstructure observations. *J. Phys. Oceanogr.* **31**, 1969–1992.

THORPE, S. A. 1973 Experiments on instability and turbulence in a stratified shear flow. *J. Fluid Mech.* **61**, 731–751.

THORPE, S. A. 2010 Turbulent hydraulic jumps in a stratified shear flow. *J. Fluid Mech.* **654**, 305–350.

THORPE, S. A. & LI, L. 2014 Turbulent hydraulic jumps in a stratified shear flow. Part 2. *J. Fluid Mech.* **758**, 94–120; (referred to as 'TL').

VOET, G., ALFORD, M. H., GIRTON, J. B., CARTER, G. S., MICKETT, J. B. & KLYMAK, J. M. 2016 Warming and weakening of the abyssal flow through the Samoan Passage. *J. Phys. Oceanogr.* **46**, 2389–2401.

VOET, G., GIRTON, J. B., ALFORD, M. H., CARTER, G. S., KLYMAK, J. M. & MICKETT, J. B. 2015 Pathways, volume transport, and mixing of abyssal water in the Samoan Passage. *J. Phys. Oceanogr.* **45**, 562–588.

WINTERS, K. B. & ARMI, L. 2014 Topographic control and stratified flows: upstream jets, blocking and isolating layers. *J. Fluid Mech.* **753**, 80–103.

YAKOVENKO, S. N., THOMAS, T. G. & CASTRO, I. P. 2011 A turbulent patch arising from a breaking internal wave. *J. Fluid Mech.* **677**, 103–133.

YAKOVENKO, S. N., THOMAS, T. G. & CASTRO, I. P. 2014 Transition through Rayleigh–Taylor instabilities in a breaking internal lee wave. *J. Fluid Mech.* **760**, 466–493.